



**Enhancing interfacial charge transfer in WO₃/BiVO₄
photoanode heterojunction through gallium and tungsten
co-doping and sulfur modified Bi₂O₃ interfacial layer**

Journal:	<i>Journal of Materials Chemistry A</i>
Manuscript ID	TA-ART-05-2021-003786.R2
Article Type:	Paper
Date Submitted by the Author:	26-Jun-2021
Complete List of Authors:	Prasad, Umesh; Arizona State University, System engineering; Arizona State University, System engineering Young, James; National Renewable Energy Laboratory, Johnson, Justin; NREL, McGott, Deborah; National Renewable Energy Laboratory Gu, Hengfei ; Rutgers University, , Chemistry and Chemical Biology Garfunkel, Eric; Rutgers The State University of New Jersey, Chemistry and Chemical Biology Kannan, Arunachala; Arizona State University, Department of Electronic Systems

Enhancing interfacial charge transfer in WO₃/BiVO₄ photoanode heterojunction through gallium and tungsten co-doping and sulfur modified Bi₂O₃ interfacial layer

Umesh Prasad^{1,2}, James L. Young^{2*}, Justin C. Johnson², Deborah L. McGott^{2,3}, Hengfei Gu⁴, Eric Garfunkel⁴ and Arunachala M. Kannan^{1*}

¹The Polytechnic School, Ira A. Fulton Schools of Engineering, Arizona State University, Mesa, AZ 85212, USA

²National Renewable Energy Laboratory, Golden, CO 80401, USA

³Colorado School of Mines, Golden, CO, 80401, USA

⁴Department of Chemistry and Chemical Biology, Rutgers University, Piscataway, NJ 08854, USA

Abstract

Photoanodes containing a WO₃/BiVO₄ heterojunction have demonstrated promising photoelectrochemical water splitting performance, but the ability to effectively passivate the WO₃/BiVO₄ interface has limited charge transport and collection. Here, the WO₃/BiVO₄ interface is passivated with a sulfur-modified Bi₂O₃ interfacial layer with staggered band edge alignment to facilitate charge transfer and lifetime. Additionally, BiVO₄ was co-doped with Ga³⁺ at Bi³⁺ sites and W⁶⁺ at V⁵⁺ sites (i.e., (Ga,W):BiVO₄) to improve the light absorption and photogenerated charge carrier concentration. The optimized WO₃/S:Bi₂O₃/(Ga,W):BiVO₄ photoanode exhibited a photocurrent of 4.0±0.2 mA.cm⁻² compared to WO₃/(Ga,W):BiVO₄ with 2.8±0.12 mA.cm⁻² at 1.23 V_{RHE} in K₂HPO₄ under simulated AM 1.5G illumination. Time-resolved photoluminescence spectroscopic analysis of the WO₃/S:Bi₂O₃/(Ga,W):BiVO₄ electrode validated the enhanced interfacial charge transfer kinetics. In *operando* femto- and nano-second transient absorption spectroscopy confirmed the presence of long-lived photogenerated charge carriers and revealed lower recombination initially due to rapid charge separation for WO₃/S:Bi₂O₃/(Ga,W):BiVO₄. The distribution and role of sulfur was further investigated using EDAX, XPS and TOF-SIMS depth profiling. Finally, a Co-Pi co-catalyst layer was added to achieve photocurrent 5.1±0.25 mA.cm⁻² and corresponding H₂ generation rate 67.3 μmol.h⁻¹cm⁻² for WO₃/S:Bi₂O₃/(Ga,W):BiVO₄/Co-Pi photoanode.

Keywords: Bismuth vanadate, thin-film, interface layer, TOF-SIMS, TAS, depth profiling, photoelectrochemical water splitting

*Corresponding Authors: Email amk@asu.edu, james.young@nrel.gov

1. Introduction

Hydrogen generation by solar assisted photocatalytic water splitting is an attractive route to store solar energy in the form of chemical fuels.¹⁻³ For such an application, efficient photon harvesting semiconducting oxides have been studied extensively due to their superior electrochemical stability, low cost and natural abundance.³ Monoclinic n-type bismuth vanadate (BiVO_4) is a promising semiconductor for oxygen evolution reactions (OER).⁴ It possesses a bandgap of ~ 2.4 eV, conduction band (CB) edge close to 0 volt vs reversible hydrogen electrode (V_{RHE}) and deep valence band (VB) position ($\sim 2.4 V_{\text{RHE}}$) that generate the substantial thermodynamic driving force for oxygen evolution.^{5,6} The effective defect-tolerant nature⁵ with moderate charge transport properties facilitates BiVO_4 to achieve up to $\sim 7.5 \text{ mA}\cdot\text{cm}^{-2}$ theoretical photocurrent density (PCD) at $1.23 V_{\text{RHE}}$ under simulated AM 1.5G illumination ($100 \text{ mW}\cdot\text{cm}^{-2}$). However, OER properties of BiVO_4 suffer from low charge transfer rates due to excessive surface recombination in *ps-ns* time scale.^{7,8} In parallel, the desirable water oxidation occurs at a slower time scale, typically over *ms-s* range, due its four-electron reaction mechanism.^{6,7,9} Fast charge separation and transport of photogenerated electron-hole pairs are essential for efficient water oxidation.^{8,10} Several strategies have been employed to enhance the charge separation and transfer such as composition tuning or doping,^{5,10} formation of homo- and hetero- junctions,^{5,11,12} passivation layer¹³ and co-catalyst.¹⁴ Tungsten (W) and molybdenum (Mo) have been extensively studied as donor-type dopants in BiVO_4 to increase charge carrier density, mobility and minimize recombination pathways at solid/solid and solid/electrolyte interfaces.^{11,15} Along with composition tuning, forming heterojunction, in particular, type-II heterojunction formation between WO_3 (bandgap: 2.7 eV, VB: 0.4 eV & CB: 3.1 eV) and BiVO_4 (VB: 0.02 eV & CB: 2.4 eV) is efficient due to appropriate band alignment, which promotes spatial charge separation and relatively better charge transfer by providing substantial thermodynamic driving force and interfacial electric field.^{6,16} However, the

WO₃/BiVO₄ heterojunction suffers from slow charge transfer (sub μ s) from BiVO₄ to WO₃ due to poor charge transport properties of BiVO₄ and the presence of recombination centers at the heterojunction interface.^{8,17} For such issues, adding an interfacial layer between the WO₃/BiVO₄ heterojunction is a promising approach to reduce the interfacial charge recombination and promote charge transfer.

In the present study, a multifaceted approach was implemented for addressing the interfacial charge recombination in WO₃/BiVO₄ heterojunction where (i) BiVO₄ was co-doped and (ii) an interfacial layer was implemented to improve the effective charge separation and transfer. Initially, BiVO₄ was co-doped with Ga³⁺ and W⁶⁺ at the Bi³⁺ and V⁵⁺ sites, respectively, to enhance light absorption, concentration of photogenerated charge carriers, and improve bulk charge separation. A uniquely prepared sulfur (S) modified Bi₂O₃ (S:Bi₂O₃) layer was implemented so that S diffused to adjacent underlayer (WO₃) and overlayer ((Ga,W):BiVO₄), which helped in increasing additional reactive sites for charge transport. Energy-dispersive X-ray analysis (EDAX), X-ray photoelectron spectroscopy (XPS) and time-of-flight secondary ion mass spectrometry (TOF-SIMS) depth profiling determined the qualitative and uniform distribution of sulfur in all layers. The PCD increased from 2.8±0.12 to 4.0±0.2 mA.cm⁻² for WO₃/(Ga,W):BiVO₄ and WO₃/S:Bi₂O₃/(Ga,W):BiVO₄, respectively. Additionally, the photocurrent improved to 5.1±0.25 mA.cm⁻² after adding cobalt phosphate (Co-Pi) to yield a hydrogen collection rate of 67.3 μ mol.h⁻¹cm⁻² for WO₃/S:Bi₂O₃/(Ga,W):BiVO₄/Co-Pi photoanode at 1.23 V_{RHE} in K₂HPO₄ (KPi) under simulated AM 1.5G illumination. Time-resolved photoluminescence (TRPL) and in *operando* femto- and nano-second transient absorption spectroscopy (fs- and ns- TA) results are consistent with more holes rapidly directed to the reactive surface initially and fast electron transfer from (Ga,W):BiVO₄ to S:Bi₂O₃ in *ps-ns* and from S:Bi₂O₃ to WO₃ in *ns- μ s* time scale. From the detailed

analysis, we show that the insertion of a S:Bi₂O₃ interfacial layer resulted in the best charge separation and transfer kinetics, as well as reduced interfacial recombination sites of all architectures tested. The achieved results are among the highest reported photocurrent densities and hydrogen production rates in the literature.

2. Experimental

2.1 Thin films fabrication:

The BiVO₄ based thin films were fabricated on 1×1 cm² fluorine-doped tin oxide (FTO) glass substrate (Aldrich Chemistry: 2.3 mm thick, ~7 Ω/sq surface resistivity) using ultrasonic spray coating (Sono-Tek Corporation, USA). A precursor solution of BiVO₄ was prepared by dissolving 3mM Bi(NO₃)₃·5H₂O (Alfa-Aesar, CAS#10035060) and 3mM NH₄VO₃ (Sigma-Aldrich, CAS#7803556) in 2M HNO₃ (Sigma-Aldrich, CAS#7803556). The precursor solution was sprayed at a flow rate of 0.1 ml/min for 4 cycles over a FTO substrate held at 70°C, then annealed for 10 min at 500°C in the furnace (Thermo Scientific Thermolyne, model: F48028). The annealed film was sprayed with an additional 4 cycles for optimized film thickness and then annealed at 500°C for 2 h. Ga doping was performed by dissolving 3mM Ga(NO₃)₃·xH₂O (Sigma-Aldrich, CAS#69365726) in the BiVO₄ precursor solution to get varied Bi_{1-x}Ga_xVO₄ compositions (where x = 0.01 - 0.06 and x = 0.04 was found to be optimal) (Figure S1a). W doping was carried out non-stoichiometrically¹⁵ by mixing 3mM (NH₄)₁₀H₂(W₂O₇)₆ (Sigma-Aldrich, CAS#11140775) in the BiVO₄ precursor solution to acquire BiV_{0.992}W_{0.013}O₄ (termed W:BiVO₄). The simultaneous co-doping of Ga and W in BiVO₄ was executed by taking the required amount of gallium nitrate and ammonium tungstate in BiVO₄ precursor solution to obtain Bi_{0.96}Ga_{0.04}V_{0.992}W_{0.013}O₄ (termed (Ga,W):BiVO₄).

WO₃ films were fabricated by dissolving 3mM (NH₄)₁₀H₂(W₂O₇)₆ (Sigma-Aldrich, CAS#10031513) in 2M HNO₃ (Sigma-Aldrich, CAS#7803556). The precursor solution was sprayed for 4 cycles over FTO substrate (kept at 40°C) with a flow rate of 0.1 ml/min using an ultrasonic spray coating tool. The film was annealed at 500°C for 2 h in air to obtain a thin adherent WO₃ film. (Ga,W):BiVO₄ was then sprayed over the WO₃ film to form WO₃/(Ga,W):BiVO₄.

The precursor solution for Bi₂O₃ was prepared by dissolving 1mM Bi(NO₃)₃·5H₂O (Alfa-Aesar, CAS#10035060) in 10 ml acetic acid (Sigma-Aldrich, CAS#64197). WO₃/Bi₂O₃ film was fabricated by ultrasonically spraying Bi₂O₃ precursor on WO₃ film (kept at 70°C) for 3 cycles. The WO₃/Bi₂O₃ bilayer was then annealed at 500°C for 2 h in air. (Ga,W):BiVO₄ was subsequently sprayed (as discussed) to form WO₃/Bi₂O₃/(Ga,W):BiVO₄.

Figure 1 and S1b show a schematic of the WO₃/S:Bi₂O₃/(Ga,W):BiVO₄/Co-Pi film fabrication process. The sprayed Bi₂O₃ film was immersed in 35 ml methanol (Sigma-Aldrich, CAS#67561) and 0.4mM dibenzyl disulfide (Alfa Aesar, CAS#150607) for 20 min and then annealed in sulfur vapor using a tube furnace (Thermo Scientific Thermolyne, model: HTF55322C). Sulfur vapor was generated by heating 2.5 g of sulfur powder (Alfa Aesar, CAS#7704349) at 120°C in the tube furnace's upstream section. Argon (purity: 99.99%) was used as a carrier gas the sulfur vapor downstream where the thin film was placed in the hot zone of the tubular furnace at 445°C in air for 1 h to incorporate S in the Bi₂O₃ (termed S:Bi₂O₃). In the final step, the sulfur-rich film with WO₃ layer was used as a substrate to spray (Ga,W):BiVO₄ precursor solution and annealed in air at 500°C for 2 h to obtain WO₃/S:Bi₂O₃/(Ga,W):BiVO₄ film.

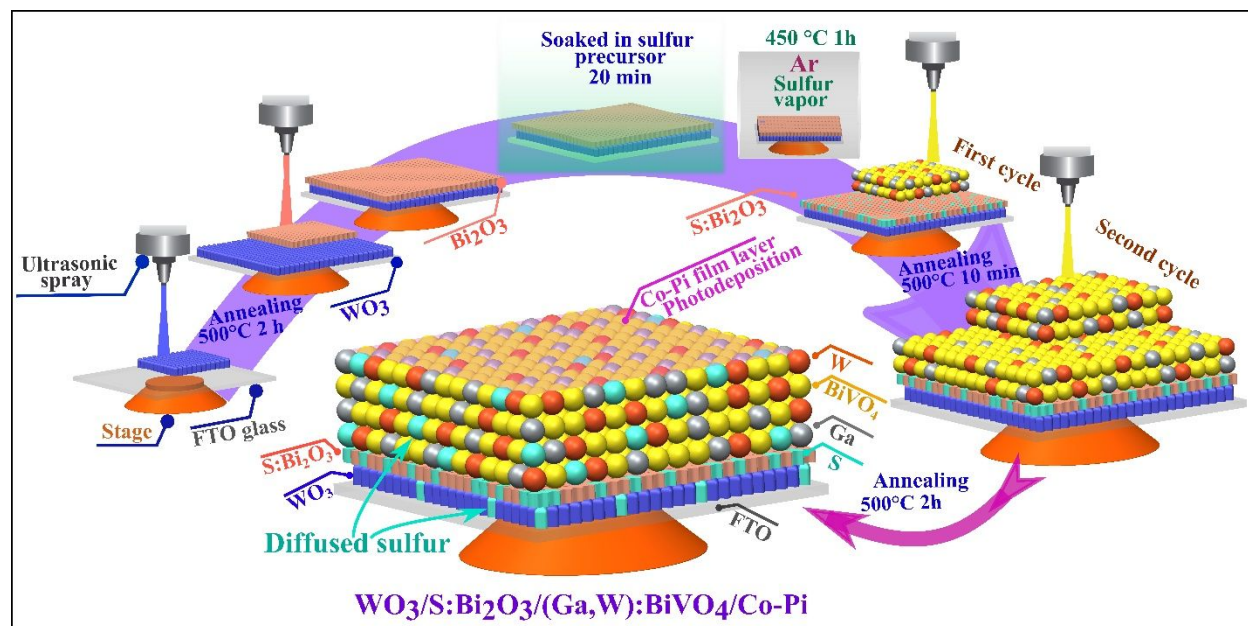


Figure 1. Schematic illustration of the $WO_3/S:Bi_2O_3/(Ga,W):BiVO_4/Co-Pi$ film fabrication process.

A co-catalyst Co-Pi was photo-electrodeposited by dissolving 0.1M K_2HPO_4 (Sigma-Aldrich, CAS#7758114) and 0.5mM $Co(NO_3)_2 \cdot 6H_2O$ (Sigma-Aldrich, CAS#10026229) in DI water at 0.71 $V_{Ag/AgCl}$ for 30 s under simulated AM 1.5G illumination to obtain $WO_3/S:Bi_2O_3/(Ga,W):BiVO_4/Co-Pi$.

2.2 Material characterization:

The morphology and elemental spatial distribution of prepared samples were characterized using a field emission scanning electron microscope (FE-SEM, JEOL 7000F) equipped with EDAX at 25 kV. To investigate the chemical migration that occurs during the sample synthesis process time of flight secondary ion mass spectrometry TOF-SIMS depth profiling was performed on films at various stages of the annealing process utilizing an ION-TOF TOF-SIMS V spectrometer. The analysis was completed using a 3-lens 30kV BiMn primary ion gun (30KeV Bi^+ analysis beam at 1pA pulsed beam current, where a $50 \times 50 \mu m$ area was analyzed while the dose density was kept

below 1×10^{12} ions cm^{-2} to remain under the static SIMS limit. Sputter depth profiling was accomplished with a 3kV cesium ion beam (20 nA sputter current) with a raster of 100×100 microns.

UV–Visible spectroscopy was carried out using Agilent Technologies (Model: Cary 6000i) optical spectrophotometer. XPS spectra were acquired with a 180° double-focusing hemispherical analyzer with a 128-channel detector using non-monochromatic Al $K\alpha$ radiation as the X-ray source (1486 eV) (Thermo Scientific™ K-Alpha™ X-ray Photoelectron Spectrometer System; VG 220i-XL). This X-ray source beam (diameter: ~ 0.4 mm) was chosen to minimize the superposition of photoelectron and Auger lines of essential elements. The energy resolution was 0.73 eV with a sufficiently small broadening of natural core level lines and a reasonable signal-to-noise ratio. The binding energy scale was calibrated about C 1s at 285 eV, giving an accuracy of 0.1 eV. For depth profiling, a Thermo K-Alpha spectrometer was used with a flood gun for charge compensation and sputtering was carried out with a raster 2 mm in diameter using Ar sputtering at 3 keV. An X-ray beam with a 35 μm diameter was used every 60 s up to 200 cycles of etching. S2s peaks were used for S concentration due to high interference between S 2p and Bi 4f peaks. However, due to the very low relative sensitivity factor of S 2s, the signal-to-noise ratio is relatively low at the given S doping level as compared to the other elements, making the error range relatively larger. TRPL measurements were taken using a setup similar to that described by Kuciauskas et al.¹⁸ A PicoQuant 405 nm diode laser-generated short pulses (pulse width: ~ 130 ps) with repetition rate 1 MHz, beam spot size 50 μm and 11 μW power. A fibre-coupled avalanche photodiode with a timing resolution of 40 ps was used as the detector. Photon counting rate was maintained at approximately 1% of the repetition rate. Lifetime values were calculated by fitting the decay section of each curve with a biexponential function.

Femto- and nano-second transient absorption spectroscopy (fs- and ns- TAS) was conducted with a Helios Fire spectrometer (Ultrafast Systems), employing a Pharos amplified laser (Light Conversion) as the excitation source. The Pharos was operated at 4 kHz and 4 W power, along with a small portion directed to a sapphire crystal to generate the supercontinuum probe (900–1600 nm). The pump wavelength was tuned to 430 nm with an Orpheus optical parametric amplifier and attenuated with neutral density filters to approximately 150 nJ before being directed to the sample with a spot size of ~0.5 mm. The probe was overlapped with the pump at the sample position and detected with an InGaAs photodiode array and photoinduced transmission changes were established by modulating the pump at 2 kHz and subtracting “pump off” from “pump on” probe spectra. The data were adjusted for chirp and background scatter using Surface Explorer. The *ns-ms* TA was performed with the same excitation beam but with an electronically delay supercontinuum probe (Ultrafast System, EOS) to achieve longer delay times. The *in operando* TA measurement was conducted at open circuit potential by placing sample in a quartz cell in Kpi electrolyte. Applied potential was controlled using a Pine WaveNow (Pine Research) Potentiostat/Galvanostat.

2.3 Photoelectrochemical measurements:

Photoanodes were constructed from the prepared thin films by attaching a copper wire to the FTO, and silver paint was used to establish electrical contact. Epoxy (Loctite 9460) was applied to secure the connection and cover the copper wire, silver paint, and FTO edges. The PEC performance of the photoanodes was evaluated in a standard three-electrode configuration using Pt wire (Premion 99.997%) and Ag/AgCl (3M NaCl filling solution) as a counter and reference electrodes, respectively. A solar simulator (Sun 3000, model#11000A, ABET Technologies, USA) was used as the light source. Simulated AM 1.5G illumination was established using a GaInP (bandgap: 1.8 eV) photovoltaic primary reference cell. Potentiostat/galvanostat (BioLogic SP-300) was used for

photoelectrochemical (PEC) measurements in 0.1 M KPi solution in water (pH = 8.0). The electrolyte was degassed with N₂ gas for about 20 min before every measurement. Incident photon-to-current efficiency (IPCE) measurement was conducted using a 300 W Xe lamp (Newport, 66883), monochromator (Acton SpectraPro-150), mono-Si cell (Hamamatsu) and potentiostat (VersaSTAT 4 Ametek, Princeton Applied Research) with a lock-in amplifier (SR530 Stanford Research System). A 495 nm longpass filter (Newport) was added after the monochromator for wavelengths > 550 nm to filter second-order diffraction. Electrochemical impedance spectroscopy (EIS) measurements were performed at a frequency range of 100 kHz to 100 mHz under simulated AM 1.5G illumination.

The H₂ and O₂ gases generated in the PEC process were collected in a three-electrode setup by tracking the electrolyte volume from a filled tube.¹⁹ The faradaic efficiency (η_{H_2}) was calculated using,

$$\eta_{H_2} = \frac{\frac{P_{H_2}V}{RT}}{(Columbs\ passed) \times \left(\frac{mol\ e^-}{96485C}\right) \times \left(\frac{mol\ H_2}{2mol\ e^-}\right)}$$

Where P_{H_2} , V, R and T are pressure from H₂ evolution (hPa), volume (L), gas constant (0.08206 L atm K⁻¹mol⁻¹) and T temperature (K), respectively. P_{H_2} was calculated by subtracting the water vapor pressure ($P_{H_2O\ vapor}$) and pressure from the suspended solution ($P_{suspended}$) from atmospheric pressure (P_{atm}) measured using a barometer.

$$P_{H_2} = P_{atm} - P_{H_2O\ vapor} - P_{suspended}$$

Where, $P_{suspended}$ is calculated by measuring the height (h_1) of the suspended solution above the solution level in the setup:

$$P_{suspended} = h_1 \times \frac{Hg \text{ Density}}{Solution \text{ density}} \times \frac{1 \text{ atm}}{760 \text{ mm Hg}} = h_1 \times 0.0736 \text{ (torr}^{-1}\text{mm}^{-1}\text{)}$$

The faradic efficiency measurement was validated using Pt electrodes as an anode and cathode for the electrolysis and obtained η_{H_2} 0.98±0.02. The measurement was conducted at 1.23 V_{RHE} in KPi electrolyte under simulated AM 1.5G illumination.

3. Results and discussion

3.1. Photoelectrochemical and optical measurements

Looking first at films, Figure 2a and Table S1a compare the PEC performance of intrinsic BiVO₄ (i-BiVO₄), Ga:BiVO₄, W:BiVO₄ and (Ga,W):BiVO₄ under chopped light up to 2.4 V_{RHE}. Ga:BiVO₄ exhibited 0.4±0.02 mA.cm⁻², which is almost twice that of the i-BiVO₄ (0.25±0.01 mA.cm⁻²); this improvement is attributed to increased Fermi-level splitting and therefore decreased carrier recombination, via incorporation of Ga³⁺ at Bi³⁺ sites.²⁰ Similarly, W:BiVO₄ exhibited enhanced PCD (1.02±0.04 mA.cm⁻²) of over four times that of i-BiVO₄, which is attributed to increased carrier concentration from W⁶⁺ donors at V⁵⁺ sites.²¹ Finally, (Ga,W):BiVO₄ demonstrated superior (~ 7 times) PEC performance (1.68±0.1 mA.cm⁻²) compared to i-BiVO₄, likely due to the combined effects of Ga and W doping.

Next, PEC performance of heterojunctions was evaluated (Figures 2b, S2a and Table S1b). Based on Figure 2a, (Ga,W):BiVO₄ was selected to form a type-II heterojunction with WO₃. By doing so, WO₃/(Ga,W):BiVO₄ photoanode showed 2.8±0.12 mA.cm⁻² photocurrent, nearly doubled compared to (Ga,W):BiVO₄, likely due to improved light absorption at $\lambda \leq 450$ nm, charge transfer kinetics and reduced recombination sites.^{22,23} However, the WO₃/BiVO₄ interface is also known to have a high defect density, which can lead to significant recombination and slow charge transport.^{8,17} Therefore, a thin layer of bismuth oxide (Bi₂O₃) was inserted at the WO₃/BiVO₄ interface. While Bi₂O₃ has appropriate band alignment to promote charge transfer (validated in

Figure S2b), the PEC was not significantly enhanced relative to $\text{WO}_3/(\text{Ga,W})\text{:BiVO}_4$ (only 1.2 times higher), likely due to the higher levels of recombination in this layer.²⁴ Therefore, sulfur (S) was incorporated into the Bi_2O_3 such that, along with passivating the Bi_2O_3 bulk, S also diffused into the adjacent WO_3 and $(\text{Ga,W})\text{:BiVO}_4$ layers (Figure 2b and S2c). Sulfur is expected to enhance water oxidation by generating oxygen vacancies and forming new reaction sites that help charge migration/separation and reduce carrier recombination.^[25,26] The optimized $\text{WO}_3/\text{S}:\text{Bi}_2\text{O}_3/(\text{Ga,W})\text{:BiVO}_4$ photoanode demonstrated an excellent photocurrent of $4.0 \pm 0.2 \text{ mA}\cdot\text{cm}^{-2}$ at $1.23 \text{ V}_{\text{RHE}}$ which was ~ 1.2 and ~ 1.5 times higher than the $\text{WO}_3/\text{Bi}_2\text{O}_3/(\text{Ga,W})\text{:BiVO}_4$ and $\text{WO}_3/(\text{Ga,W})\text{:BiVO}_4$ photoanodes, respectively.

A surface catalyst (Co-Pi) deposited $\text{WO}_3/\text{S}:\text{Bi}_2\text{O}_3/(\text{Ga,W})\text{:BiVO}_4/\text{Co-Pi}$ photoanode exhibited a remarkably high photocurrent $5.1 \pm 0.25 \text{ mA}\cdot\text{cm}^{-2}$ at $1.23 \text{ V}_{\text{RHE}}$ in KPi. The Co-Pi layer facilitates hole collection at the photoanode/electrolyte interface to participate in the water oxidation reaction.⁵ The photocurrent measurement with the hole scavenger and the Mott-Schottky analysis at different frequencies are discussed in SI (Section 3 and 4).

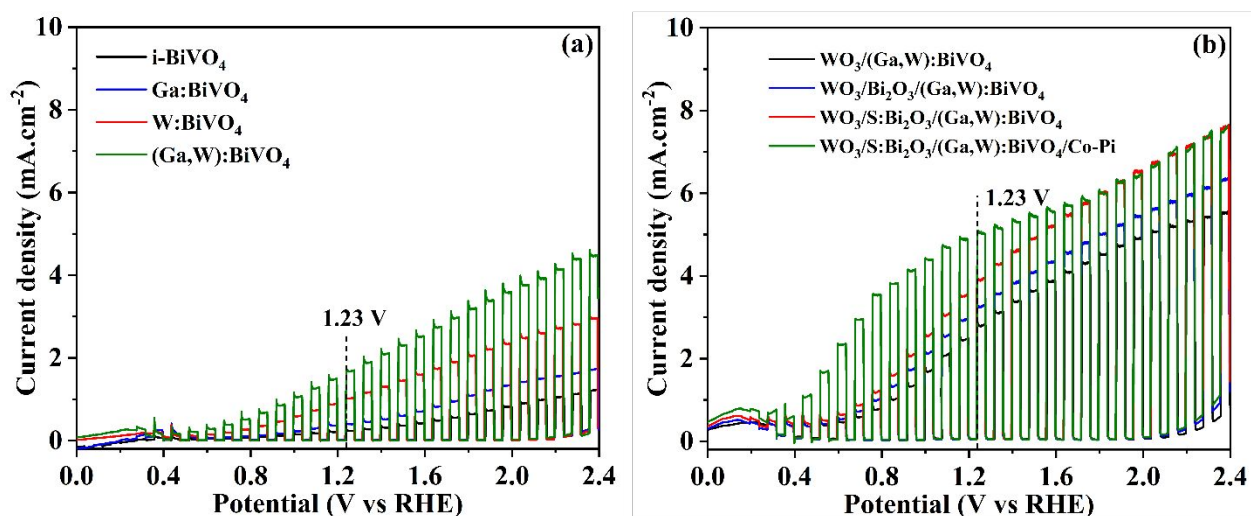


Figure 2. J - V plots under simulated AM 1.5G illumination in KPi for photoanodes (a) Ga, W doped and (Ga,W) co-doped along with $i\text{-BiVO}_4$, (b) with WO_3 heterojunction and Bi_2O_3 interface layer without and with sulfur modification.

The spectral response was investigated to understand the impact of doping, co-doping and heterojunction formation. From Figure S5a, it was observed that doping BiVO₄ with Ga enhanced total light absorption and extended the onset from ~520 to ~535 nm. A similar trend was observed for the co-doped (Ga,W):BiVO₄ sample, likely due to the redshift in light absorption caused by Ga doping.²⁰ There was no substantial change in absorption observed for W doping.¹⁰ Moreover, the light interaction improved by forming a heterojunction with WO₃ (i.e., WO₃/(Ga,W):BiVO₄) where WO₃ ($\lambda \leq 450$ nm) absorbs high energy photons along with modified BiVO₄ (300 – 530 nm), which absorb a wide range of photons. S:Bi₂O₃ ($\lambda \leq 430$) further improved the light interaction for WO₃/S:Bi₂O₃/(Ga,W):BiVO₄ compared to WO₃/Bi₂O₃/(Ga,W):BiVO₄ due to the formation of interband on S modification which causes the redshift in the light absorption.^{24,25} The respective absorption efficiency (ϕ_{abs}) was calculated by integrating the absorption spectra from 300 to 550 nm for all samples and indicated in Figure 3a and S5a: inset. The measured bandgaps were 2.71 and 2.8 eV (Figure S5b) for WO₃ and Bi₂O₃, respectively. There was a slight (~0.04 eV) reduction in the optical bandgap for Ga:BiVO₄ (2.39 eV) and (Ga,W):BiVO₄ (2.38 eV) compared to i-BiVO₄ (2.42 eV), which was expected due to the redshift in the absorption edge on Ga doping. Bulk charge separation and surface charge transfer efficiencies are discussed in SI (section 5, Figure S5 c-f).

The quantification of absorbed photons undergoing photoactivity corresponding to wavelength was determined by the IPCE. The measurement for all heterojunction based photoanodes was conducted at 1.23 V_{RHE} (Figure 3b). WO₃/S:Bi₂O₃/(Ga,W):BiVO₄ photoanode showed maximum IPCE value 63±3% followed by WO₃/Bi₂O₃/(Ga,W):BiVO₄ (52±2%) and WO₃/(Ga,W):BiVO₄ (42±1.6%), respectively at 460 nm. The WO₃/S:Bi₂O₃/(Ga,W):BiVO₄ photoanode with Co-Pi exhibited the highest IPCE (72±3.2%). The IPCE was integrated over the AM1.5G reference

spectrum, and the resulting photocurrent densities for each sample (Figure 3b) agreed with those measured under simulated AM 1.5G illumination at 1.23 V_{RHE} (Figure 2b). The small variation ($\sim 5\%$) in the photocurrents measured by LSV and integrated current from IPCE is a general phenomenon due to measuring uncertainty.

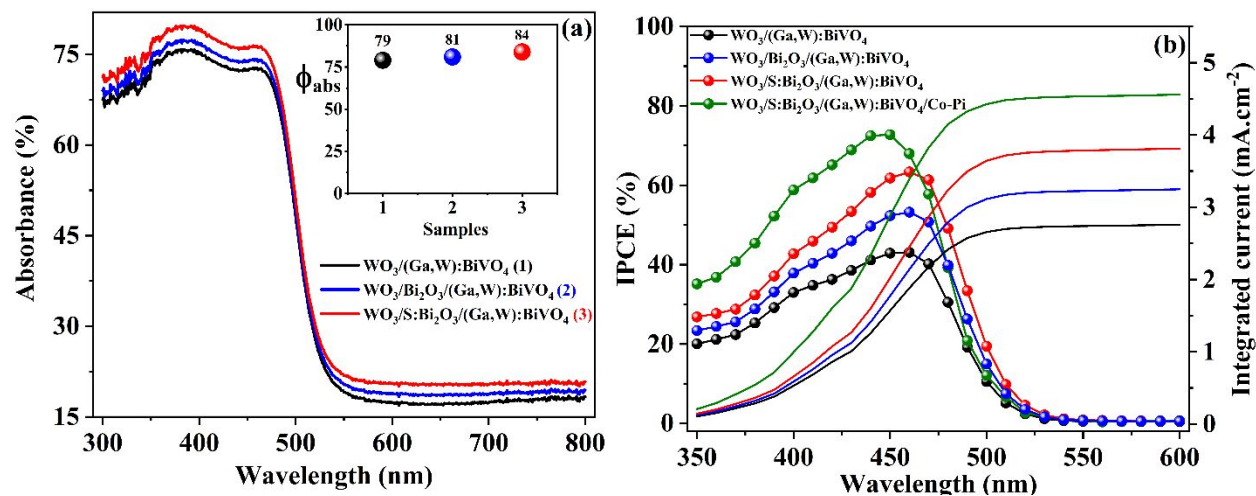


Figure 3. (a) Absorption spectra (inset: absorption efficiency), (b) incident photon-to-current efficiency, measured at 1.23 V_{RHE} in KPi electrolyte for photoanodes with WO_3 heterojunction and Bi_2O_3 interface layer without and with sulfur modification.

3.2 Surface morphology, crystal structure and elemental analysis of thin films

To better understand the PEC performance trends, the physicochemical characterization of intrinsic and doped samples was carried out to evaluate morphology, elemental mapping, crystal structure and oxidation state. The SEM images in Figure S6a-c reveal that $i-BiVO_4$, WO_3 and Bi_2O_3 have a planar structure with uniform nanoporous morphology. Figure 4a shows that after co-doping the $i-BiVO_4$ film with Ga and W, the overall porosity increased substantially without changing the grain size (50 – 200 nm). The inset image illustrates the uniform growth of nano-size grains, leading to better light absorption and more electrochemical active surface area by increasing the contact area between film surface and electrolyte. The cross-section image (Figure 4b) for $WO_3/S:Bi_2O_3/(Ga,W):BiVO_4$ demonstrated the uniformly connected nanoporous grains.

The layers thicknesses are 200-300, 200-300 and 500-750 nm for the WO_3 , $\text{S:Bi}_2\text{O}_3$ and $(\text{Ga,W})\text{:BiVO}_4$ layers, respectively. It was observed that clear separation of all three layers is difficult as layers amalgamated due to the porous nature of all films. The FTO coating thickness on the glass substrate was ~ 50 nm (Figure S6d). The composition and elemental distribution of as-deposited $\text{WO}_3/\text{S:Bi}_2\text{O}_3/(\text{Ga,W})\text{:BiVO}_4$ were mapped based on the integrated intensities of peak Bi, V, O, W, Ga and S signals as a function of beam position using FESEM-EDAX mode. Figure 4c-h reveals the uniform distribution of elements Bi, V, O, W, Ga, and S. Consequently, the element spectra in Figure 4i demonstrates the uniform presence of S along with other elements. In Figure 4i inset, Bi and S peaks were deconvoluted to determine the distinct measure of S due to the near overlap of the two peaks. S and Bi peaks were determined at 2.36 and 2.45 keV, respectively. Additionally, the quantification of S was determined to be 2.77 at% from EDAX analysis (Figure 4i: inset).

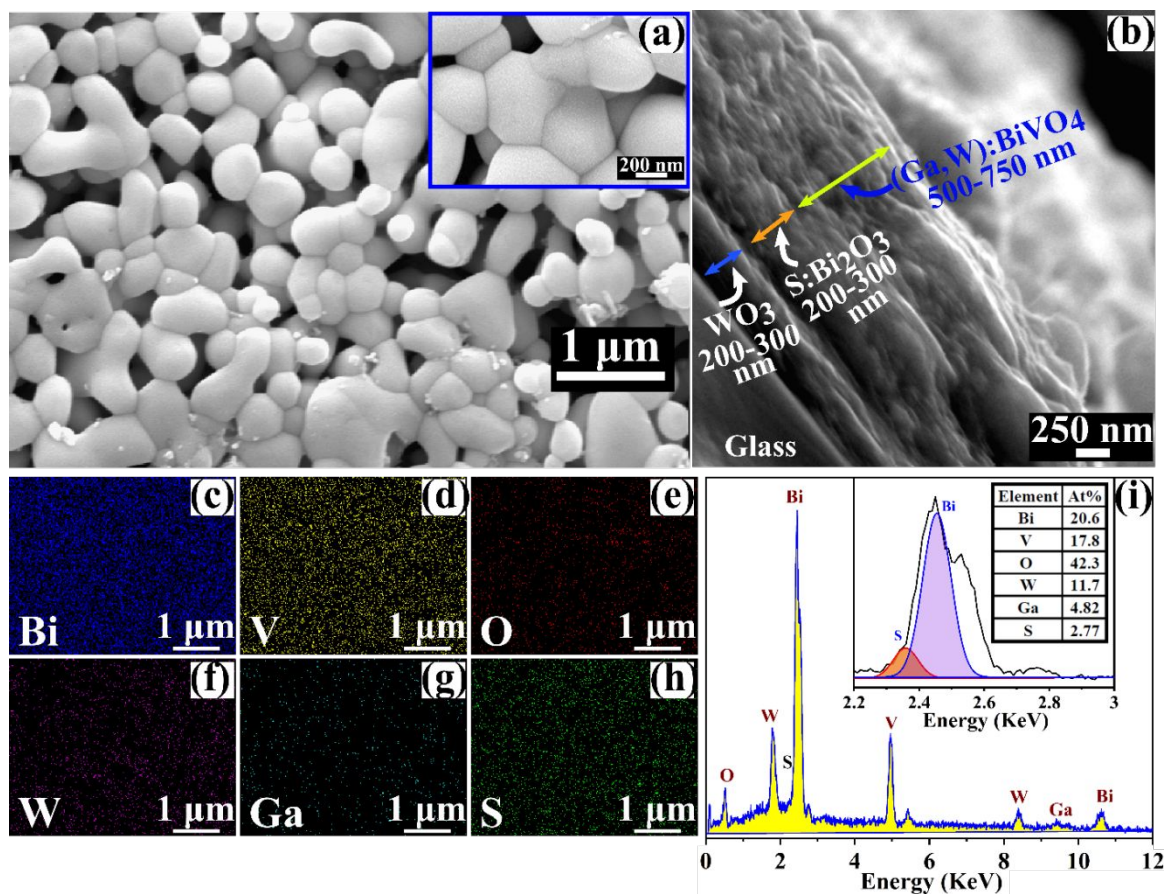


Figure 4. (a) Surface morphology. (b) Cross-section, (c-h) plan view elemental mapping and (i) elemental spectra (inset: deconvolution of Bi and S peaks and at%) of $\text{WO}_3/\text{S}:\text{Bi}_2\text{O}_3/(\text{Ga},\text{W}):\text{BiVO}_4$ sample.

The crystal structure was determined using X-ray diffraction (XRD) analysis for intrinsic, doped BiVO_4 , Bi_2O_3 , WO_3 and heterojunction samples without any impurity, complex phases and S peaks (discussed in SI, Figure S7a and S7b). The oxidation state of Bi, V, W, Ga and O in $\text{WO}_3/\text{S}:\text{Bi}_2\text{O}_3/(\text{Ga},\text{W}):\text{BiVO}_4$ sample was determined using surface XPS (discussed in SI, Figure S8a-f). However, subsequently employed XPS depth profiling could not identify S in any layers due to the low concentration of S and detection limit of XPS (Figure S8g). In order to determine the oxidation states of sulfur, two distinct samples were prepared (Figure S8h): an intermediate S treated $\text{WO}_3/\text{Bi}_2\text{O}_3$ and $\text{WO}_3/\text{S}:\text{Bi}_2\text{O}_3/(\text{Ga},\text{W}):\text{BiVO}_4$ with high S content (total S treatment to $\text{WO}_3/\text{Bi}_2\text{O}_3$ layer was 4 hrs, 4 times than actual sample). From the S 2s spectrum in Figure 5a, the

oxidation state of S was attributed to -2 in the form of Bi_2S_3 (224.8 eV) and Bi_2O_3 (230.6 and 233.8 eV) peaks for S treated $\text{WO}_3/\text{Bi}_2\text{O}_3$ sample.²⁷ Similarly, $\text{WO}_3/\text{S}:\text{Bi}_2\text{O}_3/(\text{Ga,W}):\text{BiVO}_4$ sample with high S content validated -2 states (Bi_2S_3 (223.4 eV) and Bi_2O_3 (233.3 eV)). However, it is possible that peaks at 233.8 eV and 233.3 eV could also have sulfates or highly oxidized sulfur species (SO_x).²⁷ Additionally, depth profiling was performed in Figure 5b for $\text{WO}_3/\text{S}:\text{Bi}_2\text{O}_3/(\text{Ga,W}):\text{BiVO}_4$ with high S content sample to determine the atomic concentration of Bi 4f, V 2p, O 1s, W 4f, Ga 2p and S 2s with depth. It was observed that the S distribution was uniform throughout the film depth except slightly higher at the film surface. The atomic concentration of S was approximately 12 at% uniformly distributed in the sample with high S content. It may be estimated that sulfur could be approximately 3 at% uniformly distributed in the actual sample considering S diffusion rates as sulfur treatment was 4 times in high S content sample. The atomic concentration of Bi 4f, V 2p, O 1s, W 4f and Ga 2p was distributed as per the filmstack structure. The V 2p and Ga 2p was noticed to have minor diffusion in the adjacent layers, which was possible due to the porous nature of the film.

In order to understand the nature of the sulfur diffusion process in the actual film from Bi_2O_3 interfacial layer to the WO_3 and $(\text{Ga,W}):\text{BiVO}_4$ adjacent layers, TOF-SIMS depth profiling was employed for the $\text{WO}_3/\text{S}:\text{Bi}_2\text{O}_3/(\text{Ga,W}):\text{BiVO}_4$ sample in three distinct annealing conditions after $(\text{Ga,W}):\text{BiVO}_4$ precursor deposition on sulfur treated $\text{WO}_3/\text{Bi}_2\text{O}_3$ film. The prepared samples, as shown in Figure S9a, were control (without annealing), short annealing (5 min) and complete annealing (final sample). Secondary ion signals were selected which were of high intensity and represented major components of the various layers in the filmstack. These species were: Bi^- , VO^- , WO_2^- , GaO^- and S^- to represent Bi, V, W, Ga and S elements, respectively. The layers interface was not measured due to high surface roughness and it was also observed that clear distinction of

each layer was difficult (Figure 4b and 5b) due to their porous nature. However, a rough estimation was shown in Figure S9 b-d. The control sample showed that sulfur was contained to the Bi_2O_3 layer only, as observed by the pronounced peak of sulfur in the Bi_2O_3 layer in Figure 5c. Contrarily, Figure 5d demonstrated that even on short annealing of 5 min at 500°C , significant migration of sulfur has occurred as the sulfur distribution migrated significantly into the $(\text{Ga,W})\text{:BiVO}_4$ and WO_3 layers, also noted by the significant broadening of the sulfur trace. Subsequently, in Figure 5e, a completely annealed sample (2 h time at 500°C) showed that the sulfur distribution was uniform throughout the film thickness, which was also corroborated by EDAX analysis (Figure 4c-i) and XPS depth profiling (Figure 5b). However, the sulfur content was higher on the $(\text{Ga,W})\text{:BiVO}_4$ surface, possibly due to the small deposition of sulfur during migration from Bi_2O_3 layer similar behavior was observed from XPS depth profiling (Figure 5b). It was assumed that sulfur was passivated in all grain boundaries and surfaces/interfaces/defects throughout all layers, rather than being a bulk alloy element. Along with sulfur, a less extreme amount of diffusion was observed for the components Bi, V, W and Ga in the film thickness (Figure 5c-e) may be due to the highly porous nature of the film (Figure 4a) similar behavior was observed from XPS depth profiling. The distribution of the substrate elements (F^- , Sn^- and Si^-) was shown in Figure S9b-d.

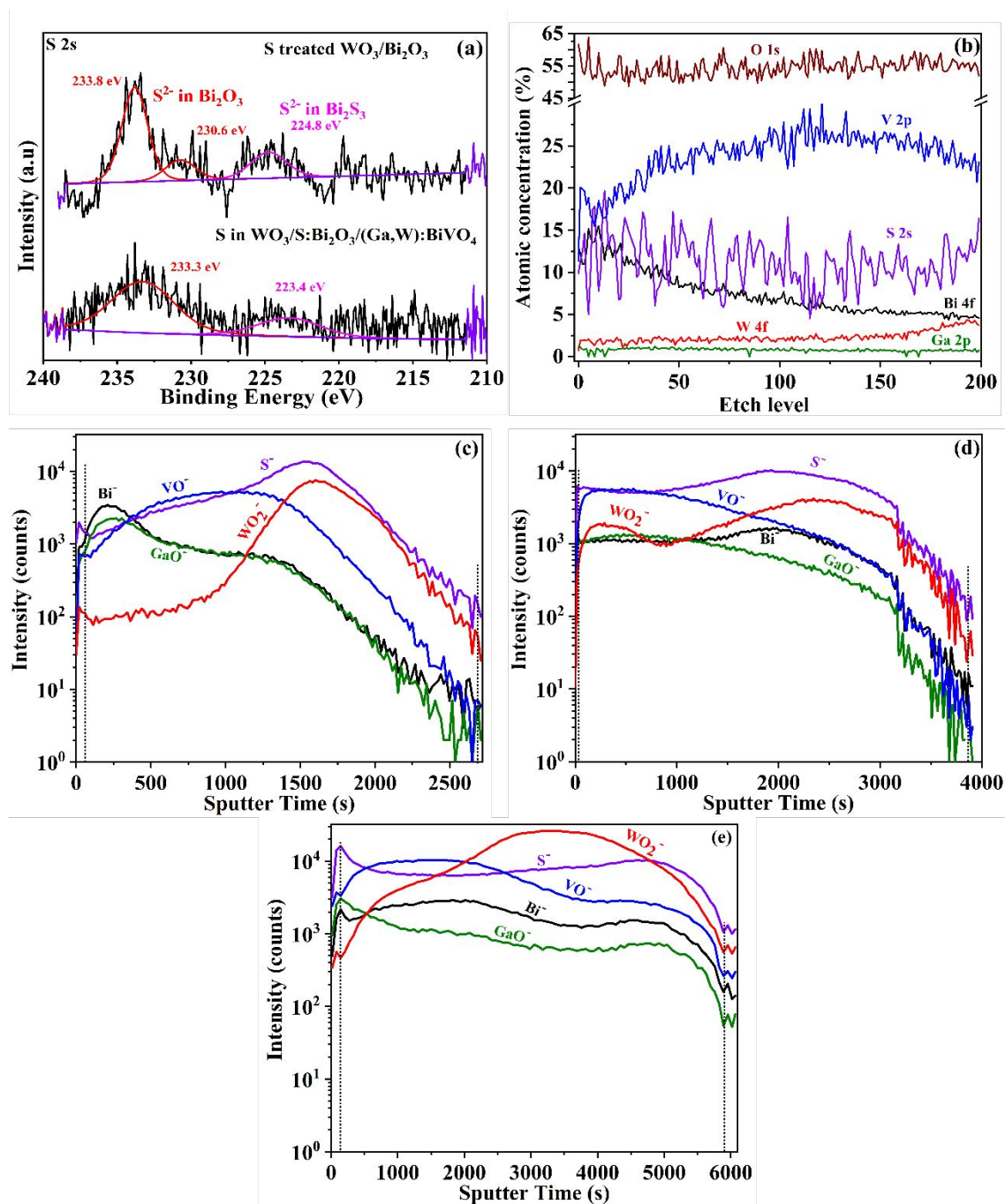


Figure 5. (a) S 2s XPS spectra of S treated $\text{WO}_3/\text{Bi}_2\text{O}_3$ and with high S concentrated $\text{WO}_3/\text{S}:\text{Bi}_2\text{O}_3/(\text{Ga},\text{W}):\text{BiVO}_4$ film. (b) XPS depth profiling spectra for atomic concentration (%) of Bi 4f, V 2p, O 1s, W 4f, Ga 2p and S 2s as a function of etch level for $\text{WO}_3/\text{S}:\text{Bi}_2\text{O}_3/(\text{Ga},\text{W}):\text{BiVO}_4$ film with high S content. Negative polarity TOF-SIMS depth profiles of $\text{WO}_3/\text{S}:\text{Bi}_2\text{O}_3/(\text{Ga},\text{W}):\text{BiVO}_4$ sample for three distinct (Figure S5a) environments (c) control (no annealing), (d) short annealing (5 min at 500°C) and (e) complete annealing (2h at 500°C) for Bi^- , VO^- , WO_2^- , GaO^- and S^- species.

3.3 Electrochemical impedance analysis

Figure 6a shows the impedance patterns of photoanodes with WO_3 heterojunction and Bi_2O_3 interface layer without and with sulfur modification. $\text{WO}_3/(\text{Ga,W})\text{:BiVO}_4$ photoanode shows lower impedance than $\text{WO}_3/\text{Bi}_2\text{O}_3/(\text{Ga,W})\text{:BiVO}_4$ at the low-frequency region. Interestingly, $\text{WO}_3/\text{S}:\text{Bi}_2\text{O}_3/(\text{Ga,W})\text{:BiVO}_4$ photoanode demonstrated even lower real impedance at a lower frequency than $\text{WO}_3/\text{Bi}_2\text{O}_3/(\text{Ga,W})\text{:BiVO}_4$. Resistance and capacitance in bulk and at the surface were evaluated as a function of voltage using Randles circuits (Figure S10a & S10b), which consists of resistance related to connections (R_{series}), bulk resistance (R_{bulk}), surface resistance ($R_{surface}$), bulk capacitance (C_{bulk}) and surface capacitance ($C_{surface}$) connected to a Helmholtz layer at the photoanode and electrolyte interface. Figure 6b shows that R_{bulk} and $R_{surface}$ tend to drop gradually until $\sim 1 \text{ V}_{\text{RHE}}$ after which, the photocurrent was mainly controlled by photogenerated holes reaching the surface.²⁸ R_{bulk} followed the order of $\text{WO}_3/\text{S}:\text{Bi}_2\text{O}_3/(\text{Ga,W})\text{:BiVO}_4 < \text{WO}_3/\text{Bi}_2\text{O}_3/(\text{Ga,W})\text{:BiVO}_4 < \text{WO}_3/(\text{Ga,W})\text{:BiVO}_4$. The evaluated capacitance of photoanodes shown in Figure 6c illustrated that C_{bulk} decreases with increasing potential and exhibits less recombination in bulk and facilitated charge transfer. The $C_{surface}$ gradually increased with potential, followed the trend $\text{WO}_3/\text{S}:\text{Bi}_2\text{O}_3/(\text{Ga,W})\text{:BiVO}_4 > \text{WO}_3/\text{Bi}_2\text{O}_3/(\text{Ga,W})\text{:BiVO}_4 > \text{WO}_3/(\text{Ga,W})\text{:BiVO}_4$. The interfacial layer with S enhanced the charge transfer rate, facilitated the charge accumulation and transport by reducing the density of surface trapped holes in the bulk and the surface.

Total resistance (R_{tot}), which represent the combination of charge transport (bulk) and interfacial charge transfer (surface), was evaluated using $R_{tot} = \left(\frac{dI}{dV}\right)^{-1}$ in Figure 6d. A valley was observed at $\sim 1 \text{ V}_{\text{RHE}}$ for all photoanodes (fitting curve was shown in Figure S10c). The cathodic shift of 164.3 and 33.5 mV in the valley implied higher charge extraction and a decrease in the R_{tot} of 39.2

and $12 \text{ } \Omega \cdot \text{cm}^{-2}$ for $\text{WO}_3/\text{S}:\text{Bi}_2\text{O}_3/(\text{Ga,W}):\text{BiVO}_4$ and $\text{WO}_3/\text{S}:\text{Bi}_2\text{O}_3/(\text{Ga,W}):\text{BiVO}_4$, respectively from $\text{WO}_3/(\text{Ga,W}):\text{BiVO}_4$) indicated the reduced bulk recombination (indicated in Figure 6b).^{28,29} Both of these criteria best fit for the $\text{WO}_3/\text{S}:\text{Bi}_2\text{O}_3/(\text{Ga,W}):\text{BiVO}_4$ photoanode confirming the higher charge separation and transfer rate. The close relationship was demonstrated by R_{tot} calculated from $I-V$ ($R_{\text{tot}} = \left(\frac{dI}{dV}\right)^{-1}$) and impedance measurement ($R_{\text{tot}} = R_{\text{bulk}} + R_{\text{surface}}$) as shown in

Figure 6d. This excellent agreement substantiates the photocurrent obtained from experiment.

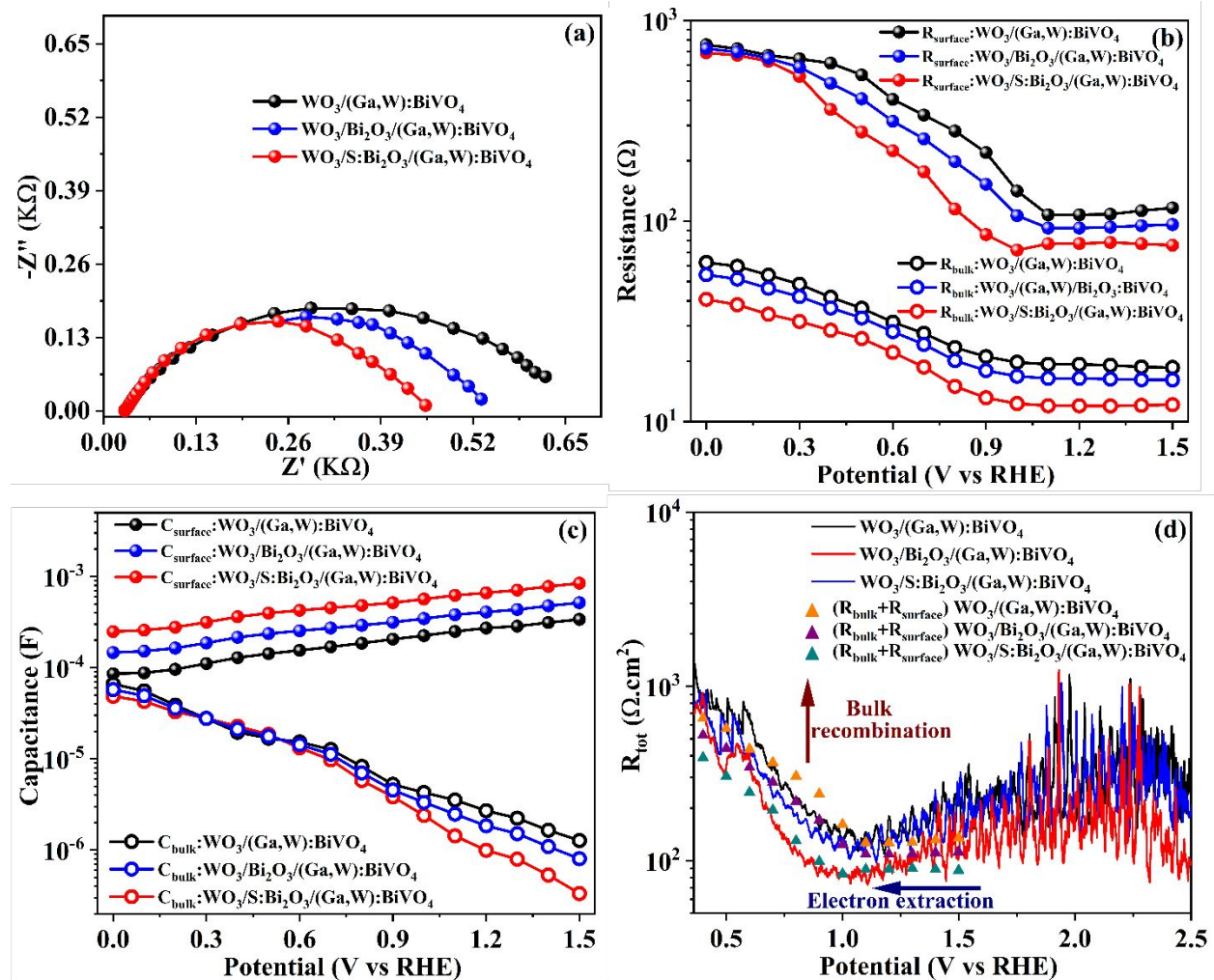


Figure 6. (a) Nyquist plots measured in KPi at $1.23 V_{\text{RHE}}$ under simulated AM 1.5G illumination, (b) R_{surface} (solid markers), R_{bulk} (open markers), (c) C_{surface} (solid markers) and C_{bulk} (open markers) determined using Randles circuit (Figure S10a & S10b) for photoanodes with WO_3 heterojunction and Bi_2O_3 interface layer without (blue) and with (red) sulfur modification. (d) R_{tot}

(line) calculated by $\left(\frac{dI}{dV}\right)^{-1}$ and compared with R_{tot} (triangles) obtained by impedance ($R_{tot}=R_{bulk}+R_{surface}$) measurement.

3.4 Time-resolved study of charge dynamics

The photogenerated charge carrier dynamics and kinetics were explored by TRPL measurement of the $\text{WO}_3/(\text{Ga,W})\text{:BiVO}_4$ and $\text{WO}_3/\text{S:Bi}_2\text{O}_3/(\text{Ga,W})\text{:BiVO}_4$ samples. Figure 7a exhibits the PL intensity decay after excitation the thick (Ga,W):BiVO₄ layer and likely produces excited states in this layer by a laser source centered at 405 nm. The PL decay ($I(t)$) was fit with a second-order exponential function $I(t) = A_1 \exp\left(-\frac{t}{\tau_1}\right) + A_2 \exp\left(-\frac{t}{\tau_2}\right)$, where A_1 and A_2 are amplitudes of components with lifetime τ_1 and τ_2 , respectively.³⁰ The average PL lifetime ($\langle\tau\rangle$) of each sample was calculated using $\langle\tau\rangle = \frac{A_1\tau_1^2 + A_2\tau_2^2}{A_1\tau_1 + A_2\tau_2}$ (all calculated parameters are presented in Table S2). The average carrier lifetimes for $\text{WO}_3/(\text{Ga,W})\text{:BiVO}_4$ and $\text{WO}_3/\text{S:Bi}_2\text{O}_3/(\text{Ga,W})\text{:BiVO}_4$ were 0.477 ± 0.05 and 0.418 ± 0.04 ns, respectively. Interestingly, the two dominant benefits which are expected from S:Bi₂O₃ incorporation (i.e., reduced recombination and fast charge transport) have competing effects on carrier lifetime, where reduced recombination increases lifetime while fast charge transport reduces it. This may be the reason that lifetime was not found to vary significantly between the two samples. The charge transfer rate constant (k_{ct}) can also be calculated as $k_{ct} = \frac{1}{\langle\tau\rangle}$.³⁰ The obtained k_{ct} for $\text{WO}_3/(\text{Ga,W})\text{:BiVO}_4$ and $\text{WO}_3/\text{S:Bi}_2\text{O}_3/(\text{Ga,W})\text{:BiVO}_4$ were 2.095 ± 0.2 ns⁻¹ and 2.393 ± 0.22 ns⁻¹, respectively, suggesting that the enhanced charge transfer may be slightly more dominant.

TA was employed for an in-depth understanding of the charge dynamics behavior across $\text{WO}_3/(\text{Ga,W})\text{:BiVO}_4$ interface without and with the S:Bi₂O₃ interfacial layer by placing the sample in the air and electrolyte (*operando*). First, fs-TA data were collected for in air, pumped at 430 nm

and probed in the range 900-1400 nm for $\text{WO}_3/(\text{Ga,W})\text{:BiVO}_4$ and $\text{WO}_3/\text{S:Bi}_2\text{O}_3/(\text{Ga,W})\text{:BiVO}_4$ samples. It is believed that this infrared probing range tracks the free and trapped photogenerated carriers, while the excitation first strikes the thick $(\text{Ga,W})\text{:BiVO}_4$ layer and likely predominately produces excited states in this layer. The intensity decay curve plotted in Figure 7b demonstrates faster initial decay on *ps* time scale for the $\text{WO}_3/(\text{Ga,W})\text{:BiVO}_4$ sample compared to $\text{WO}_3/\text{S:Bi}_2\text{O}_3/(\text{Ga,W})\text{:BiVO}_4$. This fast decay likely corresponds to geminate electron-hole recombination, which is ameliorated with the additional Bi_2O_3 layer, facilitating electron movement away from BiVO_4 and suppressing initial recombination. The recorded decay (ΔA) signal was fitted using the exponential decay model $\Delta A = \sum_{i=1}^n A_i \exp\left(-\frac{t}{\tau_i}\right)$ where A_i and τ_i are the amplitude and the lifetime of an exponential decay component, respectively. The calculated fitting parameters are summarized in Table S3, and the values are commensurate with those found in the literature.⁹ The fs-TA is best fit with 3 exponentials in the *ns* regime without an extended component in the microsecond regime due to absence of electrolyte that stabilizes separated charges. Time constant τ_1 , τ_2 and τ_3 can be inferred as loss of excited states due to hole trapping and depletion of the trapped hole due to electron-hole recombination with free and thermalized electrons.^{9,31} It is inferred from τ_1 that the initial fast processes leading to carrier loss are reduced in the $\text{WO}_3/\text{S:Bi}_2\text{O}_3/(\text{Ga,W})\text{:BiVO}_4$ sample, as all decay time constants are slower than for the $\text{WO}_3/(\text{Ga,W})\text{:BiVO}_4$ sample. The subsequent remaining carriers are left to undergo slower interfacial recombination on a *ns* timescale without electrolyte. We note that unlike TRPL, which only measures radiative electron-hole recombination and thus separation leads to reduced lifetime, the absorptive TA signal represents carrier population and as such, a persistent signal also indicates carrier motion to avoid recombination.

Next, the ns-TA measurement was conducted with samples submerged in the electrolyte to evaluate hole transfer kinetics at the semiconductor/electrolyte interface. The measurement was conducted at open circuit potential, pumped at 430 nm and probed in the range 900-1400 nm in KPi electrolyte. It was predicted that at open circuit potential, an electron trap state partially occupied can exhibit optical transition behavior to a localized trap state.⁶ The band bending at the photoanode/electrolyte interface can prolong the photogenerated holes lifetime (μs) and accumulation.⁶ This was confirmed by measuring open circuit potential (~ 0.5 and $\sim 0.55 V_{RHE}$) in the dark and flat-band potential (0.092 and $0.041 V_{RHE}$ (SI section 4)) exhibited significant band bending for $WO_3/(Ga,W):BiVO_4$ and $WO_3/S:Bi_2O_3/(Ga,W):BiVO_4$ photoanodes. From the fs-TA data described above, it is known that a larger number of holes survived the initial electron-hole recombination due to rapid charge separation/transport and subsequent transport to the reactive film surface for water oxidation reaction.^{6,16} Subsequently, from the normalized ns-TA data tracking secondary decays in Figure 7c, it was observed that $WO_3/S:Bi_2O_3/(Ga,W):BiVO_4$ exhibited slightly faster ns decay than $WO_3/(Ga,W):BiVO_4$ but otherwise had nearly identical kinetics. The recorded decay signal was fitted using the exponential decay model. The calculated fitting parameters are summarized in Table S4. The ns-TA best fit with 4 exponentials due to the presence of long-lived carriers. The shortest time scale for $WO_3/S:Bi_2O_3/(Ga,W):BiVO_4$ might represent carrier loss due to the initial, more rapid sweeping to the surface as facilitated by the additional layer. The electron extraction (K_{TA}) rate was higher for $WO_3/S:Bi_2O_3/(Ga,W):BiVO_4$ photoanode that denoted the enhanced electron mobility after placing S: Bi_2O_3 layer and impact of S diffusion to adjacent layers.

Correspondingly, the recombination between trapped holes and free electrons (τ_2) on the > 30 ns timescale was similar in $WO_3/S:Bi_2O_3/(Ga,W):BiVO_4$ (36 ns) compared to $WO_3/(Ga,W):BiVO_4$

(43 ns). The recombination of the trapped hole with thermalized electrons (τ_3) was occurring in μs range (1.1 to 1.3 μs) and expected that it would not significantly impact the overall water splitting process.¹⁶ By the time the μs timescale is reached, the leftover carriers surviving recombination have been swept far away from the internal interface, where composition is distinct between the samples, to the semiconductor/electrolyte interface where composition and thus kinetics become similar. This study provides evidence that the number of long-lived photogenerated charge carriers is improved after adding interfacial layer S:Bi₂O₃. In addition, we conclude that WO₃/S:Bi₂O₃/(Ga,W):BiVO₄ decays faster in the < 10 ns regime compared with WO₃/Ga,W):BiVO₄, suggesting improved electron transfer rate and accumulation of holes at the (Ga,W):BiVO₄ surface for water oxidation kinetics.

The primary electrons and holes separation and transfer pathways occurring among three oxides were shown in the band diagram (Figure 7d). The CB edge was determined using flat-band potential considering the negligible difference between the flat-band and bottom of CB edge.³² It was assumed that the small amount of S would not significantly change the VBs and CBs position of Bi₂O₃, WO₃ and (Ga,W):BiVO₄ layers. Being the main absorber, BiVO₄ will absorb low energy photons ($\lambda \leq 530$), while WO₃ ($\lambda \leq 450$) and S:Bi₂O₃ ($\lambda \leq 430$) will absorb high energy photons. Due to the stepped alignment and the appropriate VBs and CBs configurations, electrons can readily transport from the CBs of BiVO₄ into WO₃ via the S:Bi₂O₃ interfacial layer and into to the current collector.^{5,6} Simultaneously, photogenerated holes at WO₃ will transport to and be collected at (Ga,W):BiVO₄ through the interfacial S:Bi₂O₃ layer.

The time scales for charge separation and transport from TRPL, fs- and ns-TA analysis indicate that more holes are directed to the reactive surface on the *ps-ns* range in (Ga,W):BiVO₄. Subsequently, photogenerated electrons will transfer from S:Bi₂O₃ into WO₃ on a *ns- μs* time scale.

Recombination of photoexcited free electrons in (Ga,W):BiVO₄ is reduced by them being transferred into the CB of WO₃ via the S:Bi₂O₃ layer. Once in the WO₃, the electrons have a longer lifetime.⁸ In this process S:Bi₂O₃ play a key role in facilitating rapid charge transfer initially to WO₃ to improve the photoactivity of WO₃/S:Bi₂O₃/(Ga,W):BiVO₄ photoanode. Furthermore, the backflow of charge carriers within the photoanode is reduced by the CBs and VBs energy barriers present among the WO₃, S:Bi₂O₃ and (Ga,W):BiVO₄ layers that suppress holes and electron backflow.^[33,34,35]

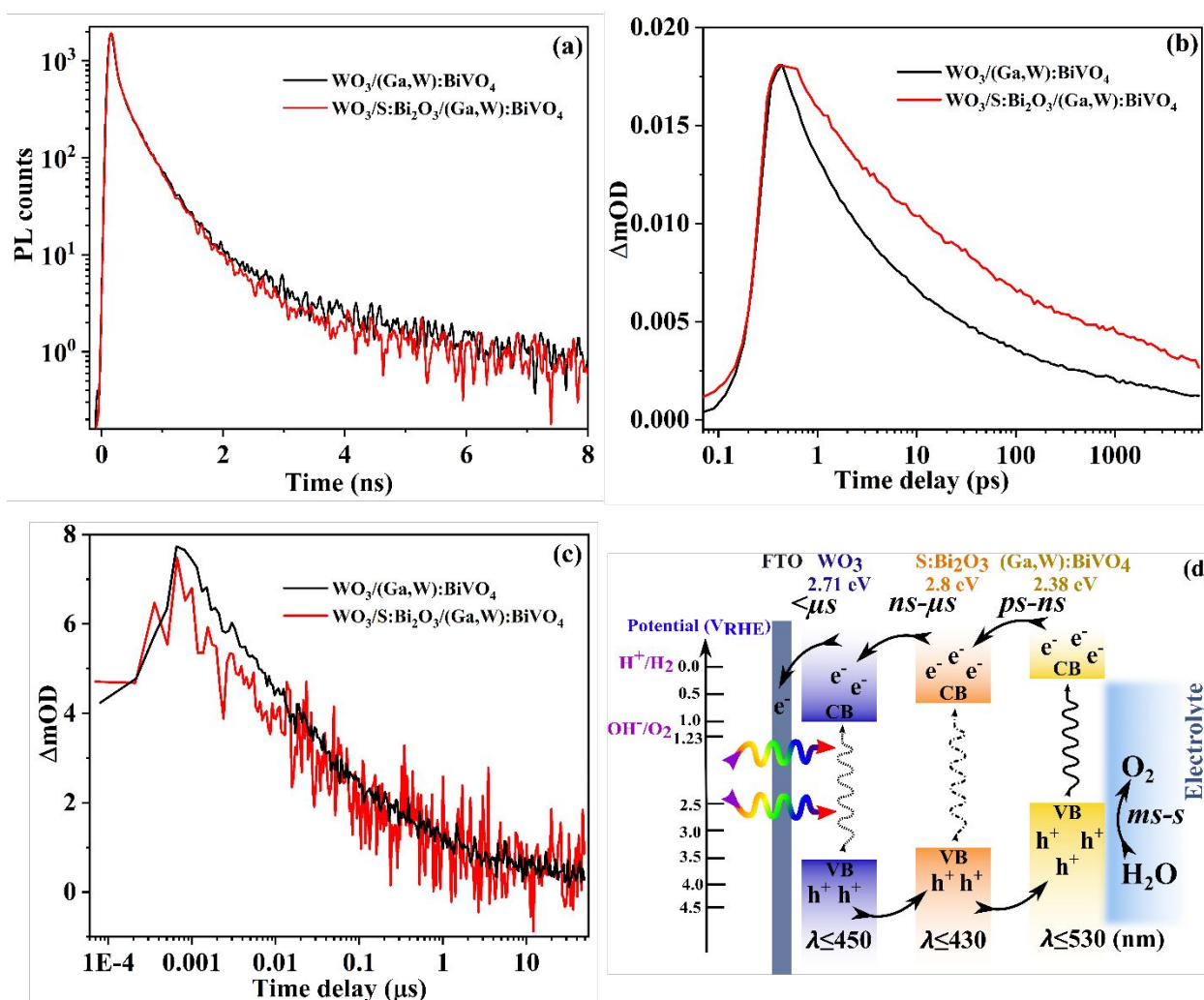


Figure 7. (a) Time-resolved PL emission (excited at $\lambda = 405$ nm). TA spectra collected, pumped at 430 nm probed in the range 900-1400 nm (b) in the air for fs-TA, (c) in KPi electrolyte for ns-TA at an open circuit potential for $\text{WO}_3/(\text{Ga,W})\text{:BiVO}_4$ and $\text{WO}_3/\text{S:Bi}_2\text{O}_3/(\text{Ga,W})\text{:BiVO}_4$

photoanodes. (d) Schematic of band alignment for $WO_3/S:Bi_2O_3/(Ga,W):BiVO_4$ heterojunction illustrating photoactivated charge generation, transfer process and related time scale.

As observed from Figure 8a, the photocurrent of all photoanodes decreases initially due to dominating photocorrosion of $(Ga,W):BiVO_4$ from the loss of V^{5+} ions in the form of V_2O_5 . However, the photocurrent further ameliorates when V_2O_5 dissolution gets saturated³⁶ as it can be observed for $WO_3/(Ga,W):BiVO_4$ photoanode, which could retain ~60% of the initial photocurrent. Further, the effect of interfacial layer Bi_2O_3 and $S:Bi_2O_3$ get more pronounced in ameliorating the charge dynamics and photocatalytic performance for $WO_3/Bi_2O_3/(Ga,W):BiVO_4$ and $WO_3/S:Bi_2O_3/(Ga,W):BiVO_4$ photoanodes by retaining ~80 and ~85 % of the initial photocurrent. Consequently, adding a protective layer Co-Pi demonstrate self-healing nature and $WO_3/S:Bi_2O_3/(Ga,W):BiVO_4/Co-Pi$ photoanode performance improve by retaining 90% of the photocurrent density compared to ~85% for $WO_3/S:Bi_2O_3/(Ga,W):BiVO_4$ photoanode after 10 h.⁵ The repeatability of photoanodes after stability measurement demonstrated no significant change in the photocurrent onset and PCD at 1.23 V_{RHE} (Figure S11). The amount of H_2 and O_2 gases generated was measured to verify the faradaic efficiency of each water splitting half-reaction. The measurement was performed for the $WO_3/S:Bi_2O_3/(Ga,W):BiVO_4/Co-Pi$ photoanode at 1.23 V_{RHE} under simulated AM 1.5G illumination in KPi electrolyte. Figure 8b shows the H_2 and O_2 gas generation rate (67.3 and 33.6 $\mu\text{mol}\cdot\text{h}^{-1}\cdot\text{cm}^{-2}$, respectively) along with the theoretical production rate and the corresponding faradaic efficiency (secondary Y-axis in Figure 8b) values (91.5 and 88%, respectively) The slightly lower values of faradaic efficiency are attributed to inhibition of proton reduction, diffusion of H_2 gases, and potential back reactions at counter electrode from dissolved O_2 .^[22,23]

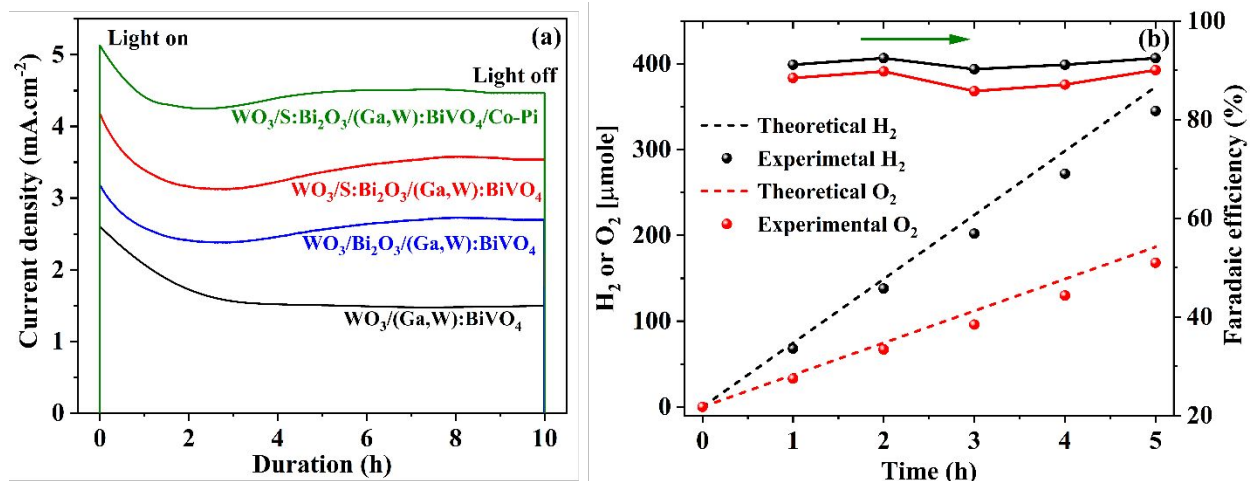


Figure 8. (a) Photoelectrochemical stability measurements of photoanodes with WO₃ heterojunction and Bi₂O₃ interface layer without and with sulfur modification. (b) Evolution of H₂ and O₂ gases for WO₃/S:Bi₂O₃/(Ga,W):BiVO₄/Co-Pi photoanode. The measurements were conducted at 1.23 V_{RHE} in KPi electrolyte under simulated AM 1.5G illumination.

Several efforts have been made by our or other groups in the field for improving interfacial passivation, charge transfer and reducing recombination sites by additional (interfacial or under/over) layer in WO₃/BiVO₄ heterojunction photoanodes. The obtained photocurrent densities at 1.23 V_{RHE} are plotted in Figure 9a. and Table S5. Choi et al.³⁷ incorporated a mild W doped BiVO₄ interfacial layer in the WO₃/BiVO₄ heterojunction for unidirectional charge flow. Zhang et al.³⁸ designed a three-story device to improve the conductivity by placing reduced graphene oxide between WO₃ and BiVO₄ layers that acted as a multichannel pathway. A Z-scheme device was designed by Wang et al.³⁹ by incorporating a W-layer between BiVO₄ and WO₃ layers for accessing holes. Beak et al.⁴⁰ used porous SnO₂ underlayer in the WO₃/BiVO₄ heterojunction where WO₃/(WO₃+SnO₂) layers formed a mixed composite for better contact and low resistance. Figure 9b and Table S6 compare hydrogen production rates at 1.23 V_{RHE} under simulated AM 1.5G illumination for BiVO₄ based heterojunction photoanodes along with the present results on

our $\text{WO}_3/\text{S}:\text{Bi}_2\text{O}_3/(\text{Ga},\text{W}):\text{BiVO}_4/\text{Co-Pi}$ photoanode. Our results are among the highest reported photocurrent densities and hydrogen production rates.

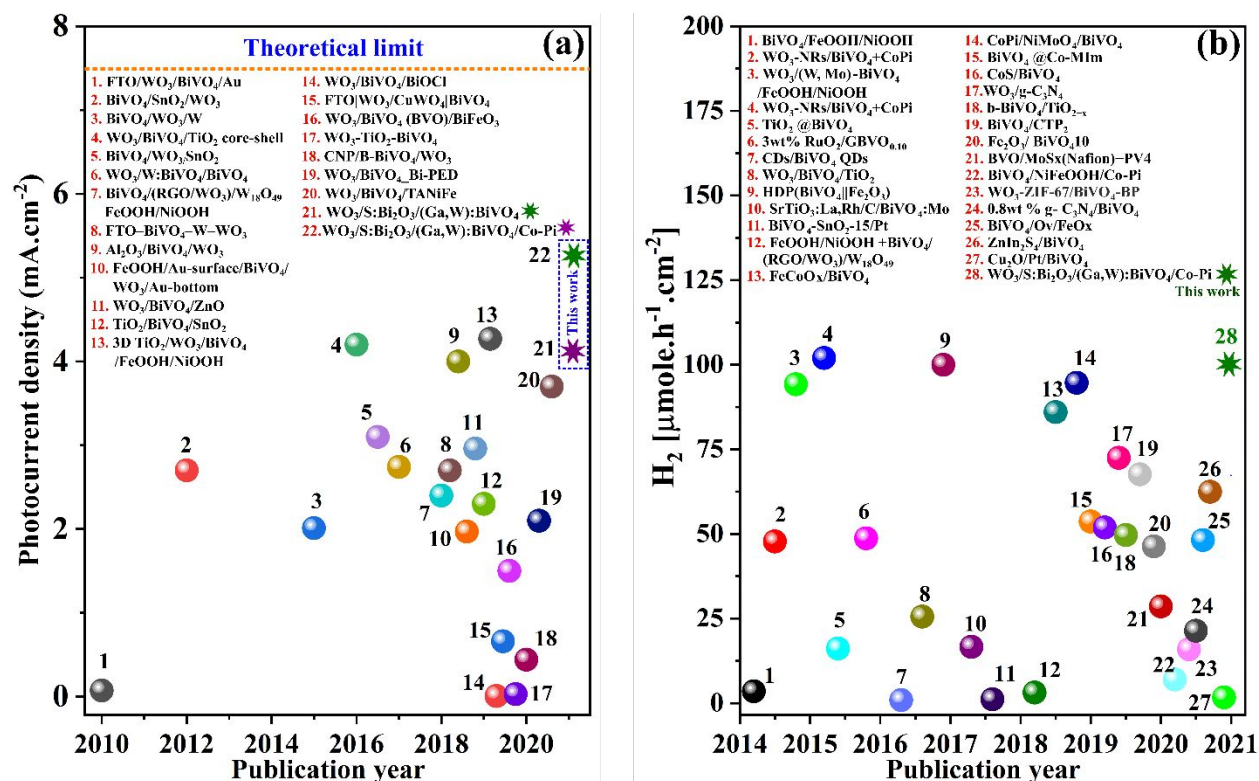


Figure 9. Comparison of (a) photocurrent density values for $\text{WO}_3/\text{BiVO}_4$ heterojunction photoanodes with additional (interfacial or under/over) layer, (b) rate of hydrogen production for BiVO_4 based heterojunction photoanodes at $1.23 V_{\text{RHE}}$ under simulated AM 1.5G illumination summarized from literature (see Table S5 in SI file), including this work.

4. Conclusion

The performance of photoanodes containing a $\text{WO}_3/\text{BiVO}_4$ heterojunction is limited, in part, by charge separation, transfer and recombination across the heterojunction interface. To mitigate these losses, a sulfur modified Bi_2O_3 interfacial layer was introduced between WO_3 and BiVO_4 layers. The BiVO_4 layer was optimized with co-doping at Bi^{3+} and V^{5+} sites by Ga^{3+} and W^{6+} , respectively, to improve the light absorption and photogenerated charge carrier extraction. The $\text{S}:\text{Bi}_2\text{O}_3$ layer between WO_3 and $(\text{Ga},\text{W}):\text{BiVO}_4$ and Co-Pi co-catalyst led to achieve $5.1 \pm 0.25 \text{ mA}\cdot\text{cm}^{-2}$ and $67.3 \text{ }\mu\text{mol}\cdot\text{h}^{-1}\cdot\text{cm}^{-2}$ photocurrent density and hydrogen collection rate for

WO₃/S:Bi₂O₃/(Ga,W):BiVO₄/Co-Pi photoanode. EDAX, XPS and TOF-SIMS depth profiling corroborated the uniform diffusion of S in all layers whereas EIS and TRPL confirmed the enhanced interfacial charge transfer kinetics. Subsequently, *operando* fs- and ns-TA analysis concluded that more long-lived photogenerated charge carriers remain after adding S:Bi₂O₃ interfacial layer, providing more holes directed to the reactive surface due to effective charge separation/transfer, and improved the overall photoanode performance. The photocurrent density and hydrogen production rates are among the highest reported for interlayer enhanced WO₃/BiVO₄ heterojunction photoanodes.

Conflicts of interest

The authors declare no conflicts of interest.

Acknowledgement

We thank Elisa M. Miller, Andrew Ferguson, Steve Johnston and Jyoti Prakash for valuable discussions and Melissa K. Gish for TA measurements. **Funding:** Financial support from Arizona State University is acknowledged. This work was authored in part by the National Renewable Energy Laboratory (NREL), operated by Alliance for Sustainable Energy, LLC, for the U.S. Department of Energy (DOE) under Contract No. DE-AC36-08GO28308. The authors acknowledge research support from the HydroGEN Advanced Water Splitting Materials Consortium, established as part of the Energy Materials Network under the U.S. Department of Energy, Office of Energy Efficiency and Renewable Energy, Fuel Cell Technologies Office, under Contract No. DE-AC36-8GO28308 to the NREL. J.C.J acknowledges the Solar Photochemistry Program of the U.S. Department of Energy, Office of Basic Energy Sciences, Division of Chemical Sciences, Biosciences and Geosciences for transient absorption experiments. The views expressed

in the article do not necessarily represent the views of the DOE or the U.S. Government. The U.S. Government and the publisher, by accepting the article for publication, acknowledge that the U.S. Government retains a nonexclusive, paid-up, irrevocable, worldwide license to publish or reproduce the published form of this work, or allow others to do so, for U.S. Government purposes.

Supporting Information

Additional Information including photoelectrochemical, Mott-Schottky, UV-vis measurements, separation and transfer efficiency calculation, SEM, XRD, XPS, TOF-SIMS, Randle circuit. Details, calculation process of theoretical photocurrent, charge transport, IPCE, APCE, integrated current, absorption efficiency evaluation. Tables including data summary, TRPL, TAS and Comparison of improved photocurrent density in $\text{WO}_3/\text{BiVO}_4$ heterojunction with an additional layer.

5. References

- 1 U. Prasad, *ACS Symp. Ser.*, 2020, **1364**, 137–167.
- 2 B. C. Xiao, L. Y. Lin, J. Y. Hong, H. S. Lin and Y. T. Song, *RSC Adv.*, 2017, **7**, 7547–7554.
- 3 T. Li, J. He, B. Peña and C. P. Berlinguette, *Angew. Chemie - Int. Ed.*, 2016, **55**, 1769–1772.
- 4 J. Prakash, U. Prasad, R. Alexander, J. Bahadur, K. Dasgupta and A. N. M. Kannan, *Langmuir*, 2019, **35**, 14492–14504.
- 5 U. Prasad, J. Prakash, X. Shi, S. K. Sharma, X. Peng and A. M. Kannan, *ACS Appl. Mater. Interfaces*, 2020, **12**, 52808–52811.
- 6 S. Selim, L. Francàs, M. García-Tecedor, S. Corby, C. Blackman, S. Gimenez, J. R. Durrant and A. Kafizas, *Chem. Sci.*, 2019, **10**, 2643–2652.
- 7 Y. Ma, S. R. Pendlebury, A. Reynal, F. Le Formal and J. R. Durrant, *Chem. Sci.*, 2014, **5**, 2964–2973.
- 8 I. Grigioni, L. Ganzer, F. V. A. Camargo, B. Bozzini, G. Cerullo and E. Selli, *ACS Energy Lett.*, 2019, **4**, 2213–2219.

- 9 I. Grigioni, M. Abdellah, A. Corti, M. V. Dozzi, L. Hammarström and E. Selli, *J. Am. Chem. Soc.*, 2018, **140**, 14042–14045.
- 10 U. Prasad, J. Prakash and A. M. Kannan, *Sustain. Energy Fuels*, 2020, **4**, 1496–1506.
- 11 J. M. Lee, J. H. Baek, T. M. Gill, X. Shi, S. Lee, I. S. Cho, H. S. Jung and X. Zheng, *J. Mater. Chem. A*, 2019, **7**, 9019–9024.
- 12 U. Prasad, J. Prakash, S. K. Gupta, J. Zuniga, Y. Mao, B. Azeredo and A. N. M. Kannan, *ACS Appl. Mater. Interfaces*, 2019, **11**, 19029–19039.
- 13 R. T. Gao, D. He, L. Wu, K. Hu, X. Liu, Y. Su and L. Wang, *Angew. Chemie - Int. Ed.*, 2020, **59**, 6213–6218.
- 14 J. Prakash, U. Prasad, X. Shi, X. Peng, B. Azeredo and A. M. Kannan, *J. Power Sources*, 2020, **448**, 227418.
- 15 U. Prasad, J. Prakash, B. Azeredo and A. Kannan, *Electrochim. Acta*, 2019, **299**, 262–272.
- 16 I. Grigioni, K. G. Stamplecoskie, E. Selli and P. V. Kamat, *J. Phys. Chem. C*, 2015, **119**, 20792–20800.
- 17 J. Su, L. Guo, N. Bao and C. A. Grimes, *Nano Lett.*, 2011, **11**, 1928–1933.
- 18 D. Kuciauskas, J. N. Duenow, A. Kanevce, J. V Li, M. R. Young, P. Dippo and D. H. Levi, in *2012 38th IEEE Photovoltaic Specialists Conference*, 2012, pp. 1721–1726.
- 19 J. L. Young, M. A. Steiner, H. Döscher, R. M. France, J. A. Turner and T. G. Deutsch, *Nat. Energy*, 2017, **2**, 1–8.
- 20 J. Xie, C. Guo and C. M. Li, *Phys. Chem. Chem. Phys.*, 2013, **15**, 15905–15911.
- 21 K. Pal, S. Parmar, J. Kang, A. Bist, P. Dua and S. Jang, *ChemSusChem*, 2012, **5**, 1926–1934.
- 22 Y. Pihosh, I. Turkevych, K. Mawatari, T. Asai, T. Hisatomi, J. Uemura, M. Tosa, K. Shimamura, J. Kubota, K. Domen and T. Kitamori, *Small*, 2014, **10**, 3692–3699.
- 23 X. Shi, I. Y. Choi, K. Zhang, J. Kwon, D. Y. Kim, J. K. Lee, S. H. Oh, J. K. Kim and J. H. Park, *Nat. Commun.*, 2014, **5**, 1–8.
- 24 X. Luo, G. Zhu, J. Peng, X. Wei, M. Hojamberdiev, L. Jin and P. Liu, *Appl. Surf. Sci.*, 2015, **351**, 260–269.
- 25 R. Wang, D. Li, H. Wang, C. Liu and L. Xu, *Nanomaterials*, 2019, **9**, 1341.
- 26 F. Han, H. Li, L. Fu, J. Yang and Z. Liu, *Chem. Phys. Lett.*, 2016, **651**, 183–187.
- 27 M. Lamers, W. Li, M. Favaro, D. E. Starr, D. Friedrich, S. Lardhi, L. Cavallo, M. Harb, R.

- Van De Krol, L. H. Wong and F. F. Abdi, *Chem. Mater.*, 2018, **30**, 8630–8638.
- 28 B. Klahr, S. Gimenez, F. Fabregat-Santiago, T. Hamann and J. Bisquert, *J. Am. Chem. Soc.*, 2012, **134**, 4294–4302.
- 29 X. Shi, I. Herraiz-Cardona, L. Bertoluzzi, P. Lopez-Varo, J. Bisquert, J. H. Park and S. Gimenez, *Phys. Chem. Chem. Phys.*, 2016, **18**, 9255–9261.
- 30 D. Kim, Z. Zhang and K. Yong, *Nanoscale*, 2018, **10**, 20256–20265.
- 31 J. Ravensbergen, F. F. Abdi, J. H. van Santen, R. N. Frese, B. Dam, R. van de Krol and J. T. M. Kennis, *J. Phys. Chem. C*, 2014, **118**, 27793–27800.
- 32 J. Resasco, H. Zhang, N. Kornienko, N. Becknell, H. Lee, J. Guo, A. L. Briseno and P. Yang, *ACS Cent. Sci.*, 2016, **2**, 80–88.
- 33 R. Saito, Y. Miseki and K. Sayama, *Chem. Commun.*, 2012, **48**, 3833–3835.
- 34 M. W. Kim, B. Joshi, E. Samuel, K. Kim, Y. Il Kim, T. G. Kim, M. T. Swihart and S. S. Yoon, *J. Alloys Compd.*, 2018, 764, 881–889.
- 35 S. Lee, J. Song, Y.-R. Jo, K. S. Choi, J. Lee, S. Seo, T. L. Kim, H. W. Jang, C. Jeon, B.-J. Kim, B. Kim and S. Lee, *ACS Appl. Mater. Interfaces*, 2019, **11**, 44069–44076.
- 36 D. K. Lee and K.-S. Choi, *Nat. Energy*, 2017, **3**, 53–60.
- 37 J. Choi, P. Sudhagar, J. H. Kim, J. Kwon, J. Kim, C. Terashima, A. Fujishima, T. Song and U. Paik, *Phys. Chem. Chem. Phys.*, 2017, **19**, 4648–4655.
- 38 Z. Zhang, B. Chen, M. Baek and K. Yong, *ACS Appl. Mater. Interfaces*, 2018, **10**, 6218–6227.
- 39 R. Wang, T. Xie, T. Zhang, T. Pu, Y. Bu and J. P. Ao, *J. Mater. Chem. A*, 2018, **6**, 12956–12961.
- 40 J. H. Baek, B. J. Kim, G. S. Han, S. W. Hwang, D. R. Kim, I. S. Cho and H. S. Jung, *ACS Appl. Mater. Interfaces*, 2017, **9**, 1479–1487.